Geophysical Journal International

Geophys. J. Int. (2016) **204,** 1134–1147 doi: 10.1093/gji/ggv494
GJI Seismology

Optimal source imaging in elastic media

Farhad Bazargani and Roel Snieder

Center for Wave Phenomena, Colorado School of Mines, Golden, CO 80401*, USA. E-mail: farhad.bazargani@gmail.com*

Accepted 2015 November 10. Received 2015 November 7; in original form 2015 July 20

SUMMARY

Time-reversal modelling provides a simple and robust solution to source-imaging problems. However, for recovering a well-resolved image of the source, time-reversal requires a balanced illumination of the target from all angles. When acquisition is incomplete and a balanced illumination is not possible, the time-reversal solution may not be adequate. We present an inversion algorithm for computing the signals to be back propagated by an array of receivers with a given configuration in order to optimally image an unknown source in an elastic medium. This approach is based on minimizing the difference between the back-propagated wavefield and the time-reversed displacement field of the source in the near source region. The proposed method requires knowledge of the propagation medium and an estimate of the source location. Other information related to the source (e.g. source mechanism) is encoded within the data and not explicitly required by the method. The method is applicable in both elastic and acoustic media. We use synthetic examples to test the performance of our method, to analyse its sensitivities, potentials and limitations and to demonstrate its potential advantages over the time-reversal source-imaging technique.

Key words: Image processing; Inverse theory; Earthquake source observations; Theoretical seismology.

1 INTRODUCTION

Earthquake source characterization is an important area of research in seismology. Characterizing seismic sources helps geophysicists understand the physics of earthquakes and faulting processes (Shearer 2009; Baig & Urbancic 2010). With the advent of hydraulic fracturing in unconventional hydrocarbon resources and with the need for monitoring the affected volume of rock in tight reservoirs, mapping and characterizing the micro-earthquakes that occur during the fracturing process has become even more important (Maxwell & Urbancic 2001; Shapiro 2008; Eisner *et al.* 2010).

Conventional methods for studying seismic sources generally involve inverting for unknown source parameters by minimizing kinematic differences between observed and simulated seismograms (Stein & Wysession 2003). Such techniques are usually performed in separate steps to first invert for source location and time and then, assuming that the source location is known, invert for the source moment tensor which completely describes the focal mechanism of the seismic source (Jost & Herrmann 1989; Baig & Urbancic 2010). More recent source inversion techniques minimize the full waveform differences between the observed data and simulated seismograms (Kim *et al.* 2011; Song & Toksöz 2011). The stability of these waveform inversion methods is limited by the acquisition geometry and the level of noise in data (Eaton & Forouhideh 2011; Song & Toksöz 2011). In particular, the solid angle subtended by the receiver array, as viewed from the source location, plays a fundamental role in the stability of the inversion; the smaller solid angles imply less stability (Eaton & Forouhideh 2011).

Time-reversal (TR) methods take an alternative approach to source characterization which is to directly image the source by back projecting seismic data into the medium (McMechan *et al.* 1985; Larmat *et al.* 2006; Kawakatsu & Montagner 2008; Lu *et al.* 2008; Artman *et al.* 2010). By comparing source-imaging and inversion methods, Kawakatsu & Montagner (2008) and Fukahata *et al.* (2014) show that the two approaches are related and that TR source imaging can be viewed as an approximation to source inversion. The underlying physical principle for TR methods is the symmetry (TR invariance) of the wave equation with respect to time in non-dissipative environments (Snieder 2002). The TR process consists of three basic steps. In the first step (forward-propagation), the wavefield generated by a source in a medium is sampled using an array of receivers. In the second step (TR), the signals recorded by the receivers are flipped in time. In the third step (back propagation), the time-reversed signals are re-injected into the medium using the same receivers which act as emitters, and are propagated back to refocus at the original source location (Fink 1997). The TR process, therefore, involves two wave propagations. These wave propagations can physically happen in a medium or the back propagation can be simulated on a computer. In a TR source-imaging experiment, the first wave propagation (forward-propagation step) physically takes place in the earth and the second wave propagation (back-propagation step) is numerically simulated on a computer.

TR source imaging and TR focusing are fundamentally related concepts. Theoretical and experimental research have proved that TR provides a simple, robust, and effective solution for focusing waves inside complex media (Fink 2006; Larmat *et al.* 2010). This

has led to application of the TR theory in many areas of science and engineering such as medical imaging (Robert & Fink 2008), underwater acoustics (Kuperman *et al.* 1998), nondestructive testing (Fink 2006) and exploration seismology (McMechan 1982).

Despite its simplicity and robustness, TR has important limitations. In theory, for a broad-band pulse emitted by an ideal point source, the returning field refocuses on a spot with dimensions of the order of the smallest wavelength (Abbe diffraction limit). This is because evanescent waves containing source details smaller than the involved wavelengths cannot be sensed in the far-field. The loss of this information causes the resolution of the process to be bounded by the diffraction limit (Fink 1997). More importantly, for proper reconstruction of the source wavefield or for effective focusing of energy onto a target point in the back-propagation step, TR requires adequate sampling of the wavefield. If this requirement is not satisfied, that is, if acquisition is incomplete and the focusing target is unevenly illuminated, which is often the case due to practical reasons, then the resolving power of TR degrades (Cassereau & Fink 1993; Fink 2006).

Several studies have been devoted to the limitations of TR modelling and offer techniques to mitigate their effects. Zhu (2014) proposes a TR modelling approach that compensates for attenuation and dispersion effects due to wave propagation in dissipative media. Research on the connection between medium complexity and the size of the focal spot has shown a direct relationship between the complexity of the medium and the resolution in TR focusing; the more complicated the medium between the source and the TR mirror, the sharper the focus (Blomgren *et al.* 2002; Fink 2008; Vellekoop *et al.* 2010). This is because when the back-propagation step is done in a real medium (or when the medium in known and the back-propagation step is simulated) a finite-aperture TR mirror acts as an antenna that uses complex environments to appear wider than it actually is, resulting in a focusing capability that is less dependent on the aperture of the TR mirror. In media consisting of a random distribution of subwavelength scatterers, a time-reversed wavefield can interact with the random medium to regenerate not only the propagating but also evanescent waves required to refocus below the diffraction limit (super-resolution). Schuster *et al.* (2012) demonstrate a method that uses evanescent waves generated by scatterers in the near-field region of seismic sources to achieve super-resolution.

To minimize the shortcomings of TR in dealing with incomplete acquisition, Tanter *et al.* (2000, 2001), Aubry *et al.* (2001) and Montaldo *et al.* (2003) introduced a focusing technique based on the inversion of the propagation operator relating an array of transducers to a set of control points inside a medium. This technique allows for calculation of the temporal signals to be emitted by each element of the array such that the injected wavefield optimally collapses on a chosen control point as a monopole field that is impulsive in time. Gallot *et al.* (2012) and Wapenaar *et al.* (2011) extended the principle of the inverse filter method to passive configuration to improve the recovery of the Green function at a defined position. They showed that application of the passive inverse filter method (compared to standard cross-correlation) helps to mitigate the problem of temporal asymmetry in the recovered Green functions due to improper spatial repartition of noise sources.

Anderson *et al.* (2015) and Douma & Snieder (2015) studied the problems caused by limited acquisition in TR source imaging and presented an alternative method for calculating an inverse signal (instead of the time-reversed signal) for back propagation. They showed that their method improves both the temporal and spatial resolution of the source images. In this paper, we extend the use of inverse signals (Douma & Snieder 2015) by taking into account that the wavefield has been sampled along different components at a number of receivers. To find the optimal signals for back propagation, we use an optimization approach that is similar to the method of Backus and Gilbert (Backus & Gilbert 1968; Tarantola 2005; Menke 2012) in inverse theory and to the inverse filter method of Tanter *et al.* (2000). However, our method is different in the sense that it (1) is a global estimator that can be used to image the seismic source and not just for locally focusing waves, and (2) it handles arbitrary source types, such as a double couple, without knowing the properties of the source. The only prerequisites of the proposed method are knowledge of the elastic medium and an estimate of the source location.

The organization of this paper is as follows: In Section 2, we develop the theory of our method for source imaging in elastic media and show how to compute signals that must be back propagated in order to optimally image a source with unknown parameters. We extend this theory for application in acoustic media in Appendix C. We then discuss how the proposed method is related to other techniques such as TR and the inverse filter method. Section 3 is devoted to a numerical example where we apply the proposed algorithm in imaging a double-couple point source. In Section 4, we use more synthetic tests to elaborate further on some explicit and implicit assumptions that are used in the construction of the proposed approach, and to analyse its sensitivity to inaccuracies in such assumptions. In Appendix B, we show that the our source-imaging method is applicable for imaging sources with finite size.

2 OPTIMIZED IMAGING OF A POINT SOURCE

Before delving into the details of our optimization method for elastic source imaging, let us define the notational conventions that are used throughout this paper.

2.1 Notation

(1) We use Einstein's notation for repeated indices: whenever an index (a subscript or a superscript) is repeated, summation over that index is implied.

(2) All superscripts are associated with the receivers and take any integer value between 1 and N.

(3) All subscripts denote spatial components.

(4) Fourier transforms follow the convention

$$f(\mathbf{x}, \omega) = \int f(\mathbf{x}, t)\, \mathrm{e}^{i\omega t}\, \mathrm{d}t. \tag{1}$$

(5) A Green tensor is 3×3 in 3-D and is 2×2 in 2-D with elements $\mathbf{G}_{np}(\mathbf{x}^i, t; \boldsymbol{\xi}, 0)$ denoting the value of the nth component of the displacement field measured at $\mathbf{x} = \mathbf{x}^i$ and time t, where the displacement field is generated by a unidirectional unit impulse parallel to the pth coordinate axis, applied at $\mathbf{x} = \boldsymbol{\xi}$ and $t = 0$.

(6) As a superscript, the asterisk $*$ denotes complex conjugation, and when the symbol is used inline, it represents the time convolution of two functions.

2.2 Formulation

Consider an elastic medium in which a single point source radiates seismic energy from an unknown location $\boldsymbol{\xi} \in W$, where W represents a subset of the medium that contains the source. (In practice,

to determine the extent of W, a rough estimate of the source location $\boldsymbol{\xi}$ is required.) We also assume that the source mechanism of the point source is described by an unknown moment tensor with an unknown time dependence $\mathbf{M}(t)$. Suppose that we sample the source displacement field $\mathbf{u}(\mathbf{x}, t)$ by N multicomponent receivers at locations $\mathbf{x}^i$. This is a passive experiment in the sense that all receivers start recording at time $t = 0$ and stop at $t = T$ such that T is large enough to allow adequate time sampling of the source displacement field $\mathbf{u}(\mathbf{x}, t)$.

Let us denote the nth component of the data vector $\mathbf{d}^i(t)$ recorded by the station at $\mathbf{x}^i$ by d_n^i. As shown by Aki & Richards (2002), this data component can be expressed as

$$d_n^i(t) = \mathbf{u}_n(\mathbf{x}^i, t) = M_{pq}(t) * \frac{\partial G_{np}(\mathbf{x}^i, t; \boldsymbol{\xi}, 0)}{\partial x_q}, \tag{1}$$

where M_{pq} denotes the elements of the source moment tensor $\mathbf{M}$, and G_{np} represents the elements of the elastodynamic Green tensor associated with the source at $\boldsymbol{\xi}$ and receiver at $\mathbf{x}^i$. In the frequency domain, eq. (1) becomes

$$d_n^i(\omega) = M_{pq}(\omega) \frac{\partial G_{np}(\mathbf{x}^i; \boldsymbol{\xi}, \omega)}{\partial \xi_q}. \tag{2}$$

The body force equivalent of the point source can be written as (Aki & Richards 2002)

$$f_n(\mathbf{x}, t) = -M_{nq}(t) \frac{\partial \delta(\mathbf{x} - \boldsymbol{\xi})}{\partial x_q}, \tag{3}$$

where δ represents the Dirac delta function. Having defined the configuration of the experiment, the data, and the body force equivalent of the point source, we are ready to formulate the optimization problem.

According to the TR process, after recording the data $\mathbf{d}^i(t)$ associated with a source, a time-reversed version of the source wavefield $\mathbf{u}(\mathbf{x}, T - t)$ can be reconstructed by broadcasting time-reversed data $\mathbf{d}^i(T - t)$ from each receiver. This process works well when the acquisition geometry of the experiment is complete and allows for adequate spatial sampling of the source wavefield. However, with incomplete acquisition, the TR process may fail to reconstruct the time-reversed source displacement field with an acceptable resolution. Therefore, in such situations, the simple process of time-reversing the data and re-injecting them is suboptimal. Our goal is to find signals $a_n^i(t)$, for each component of each receiver, such that upon injection and propagation from the receivers, the resulting injected displacement field $\boldsymbol{\psi}(\mathbf{x}, t)$ correctly reconstructs the time-reversed source displacement field $\mathbf{u}(\mathbf{x}, T - t)$.

To accomplish this goal, we define an objective function

$$J = \iint_W |\boldsymbol{\psi}(\mathbf{x}, t) - \mathbf{u}(\mathbf{x}, T - t)|^2 \, \mathrm{d}\mathbf{x} \, \mathrm{d}t, \tag{4}$$

where W denotes a subset of the medium that contains the source, $\mathbf{u}$ is the source displacement field, and $\boldsymbol{\psi}$ is the reconstructed displacement field with its components

$$\psi_n(\mathbf{x}, t) = G_{np}(\mathbf{x}, t; \mathbf{x}^i, 0) * a_p^i(t). \tag{5}$$

In writing the objective function (4), we were inspired by the so-called 'deltaness criterion' introduced by Backus & Gilbert (1968). Note that in the special case where the source is impulsive in space and time, this objective function becomes the same as the deltaness criterion in the method of Backus and Gilbert in inverse theory. For a general (nonimpulsive) source however, the objective function (4) is different from the deltaness criterion.

Following the common assumption in seismology that the source region can be considered to be locally homogeneous (Aki & Richards 2002), the particle displacements in the near-source region can be shown (Appendix A) to be proportional to the body force equivalent of the source. This proportionality makes intuitive sense because if a force is applied somewhere in an elastic medium that is locally homogeneous, then the particles pushed by the force move in the same direction as the force. Therefore, we can write

$$\mathbf{u}(\mathbf{x}, t) = C \, \mathbf{f}(\mathbf{x}, t), \tag{6}$$

where C denotes a proportionality constant with dimensions of [displacement]/[force]. Here, for simplicity, we assume $C = 1$.

Using eqs (3), (5), and (6), the objective function (4) is given by

$$J = \sum_{r=1}^{3} \iint_W \left| G_{rp}(\mathbf{x}, t; \mathbf{x}^i, 0) * a_p^i(t) + M_{rq}(T - t) \frac{\partial \delta(\mathbf{x} - \boldsymbol{\xi})}{\partial x_q} \right|^2 \mathrm{d}\mathbf{x} \, \mathrm{d}t. \tag{7}$$

In the frequency domain, this objective function can be written as

$$J(\omega) = \sum_{r=1}^{3} \int_W \left| G_{rp}^i \, a_p^i + \mathrm{e}^{i\omega T} \, M_{rq}^* \frac{\partial \delta(\mathbf{x} - \boldsymbol{\xi})}{\partial x_q} \right|^2 \mathrm{d}\mathbf{x}, \tag{8}$$

where we have used the abbreviated notation $G_{rp}^i = G_{rp}(\mathbf{x}; \mathbf{x}^i, \omega)$, $a_p^i = a_p^i(\omega)$ and $M_{rq} = M_{rq}(\omega)$.

Objective function (8) must be minimized for each frequency ω independently. To this end, we differentiate $J(\omega)$ with respect to $a_m^{n*}(\omega)$ for some particular m and n, and set $\partial J(\omega)/\partial a_m^{n*}(\omega) = 0$. This gives

$$\begin{aligned} a_p^i(\omega) \int_W G_{rm}^{n*} \, G_{rp}^i \mathrm{d}\mathbf{x} &= -\int_W \mathrm{e}^{i\omega T} \, G_{pm}^{n*} \, M_{pq}^* \frac{\partial \delta(\mathbf{x} - \boldsymbol{\xi})}{\partial x_q} \, \mathrm{d}\mathbf{x} \\ &= \int_W \mathrm{e}^{i\omega T} \, \delta(\mathbf{x} - \boldsymbol{\xi}) \, M_{pq}^* \frac{\partial G_{pm}^{n*}}{\partial x_q} \, \mathrm{d}\mathbf{x} \\ &= \mathrm{e}^{i\omega T} \, M_{pq}^* \frac{\partial G_{pm}^*(\boldsymbol{\xi}; \mathbf{x}^n, \omega)}{\partial x_q} \\ &= \mathrm{e}^{i\omega T} \, M_{pq}^* \frac{\partial G_{mp}^*(\mathbf{x}^n; \boldsymbol{\xi}, \omega)}{\partial \xi_q}, \end{aligned} \tag{9}$$

where in the last three steps of eq. (9), we used integration by parts, the sifting property of the delta function, and the reciprocity principle for the components of the Green tensor, respectively.

Next, in eq. (9), we replace indices m with n, n with i, and i with j to get

$$a_p^j(\omega) \int_W G_{rn}^{i*} \, G_{rp}^j \, \mathrm{d}\mathbf{x} = \mathrm{e}^{i\omega T} \, M_{pq}^* \frac{\partial G_{np}^*(\mathbf{x}^i; \boldsymbol{\xi}, \omega)}{\partial \xi_q}. \tag{10}$$

Comparing the right-hand side of eq. (10) with that of eq. (2), we can simplify eq. (10) as

$$a_p^j(\omega) \int_W G_{rn}^{i*} \, G_{rp}^j \, \mathrm{d}\mathbf{x} = \mathrm{e}^{i\omega T} \, d_n^{i*}(\omega). \tag{11}$$

Eq. (11) represents a linear system of equations that can be concisely expressed as

$$\boldsymbol{\Gamma}(\omega) \, \mathbf{a}(\omega) = e^{i\omega T} \, \mathbf{d}^*(\omega), \tag{12}$$

which must be independently solved for the vector $\mathbf{a}(\omega)$ for each frequency. More explicitly, eq. (12) can be written (in 3-D) as

$$\underbrace{\overset{3N\times 3N}{\begin{pmatrix}\boldsymbol{\Gamma}_{11} & \boldsymbol{\Gamma}_{12} & \boldsymbol{\Gamma}_{13}\\ \boldsymbol{\Gamma}_{21} & \boldsymbol{\Gamma}_{22} & \boldsymbol{\Gamma}_{23}\\ \boldsymbol{\Gamma}_{31} & \boldsymbol{\Gamma}_{32} & \boldsymbol{\Gamma}_{33}\end{pmatrix}}}_{\boldsymbol{\Gamma}} \underbrace{\overset{3N\times 1}{\begin{pmatrix}\mathbf{a}_1\\ \mathbf{a}_2\\ \mathbf{a}_3\end{pmatrix}}}_{\mathbf{a}} = \mathrm{e}^{i\omega T} \underbrace{\overset{3N\times 1}{\begin{pmatrix}\mathbf{d}_1\\ \mathbf{d}_2\\ \mathbf{d}_3\end{pmatrix}^{*}}}_{\mathbf{d}^{*}}, \tag{13}$$

in which the $3N \times 3N$ matrix $\boldsymbol{\Gamma}$ consists of nine $N \times N$ submatrices $\boldsymbol{\Gamma}_{kl}$ defined as

$$\Gamma_{kl}^{ij} = \int_W G_{rk}^{i*}\, G_{rl}^{j}\, \mathrm{d}\mathbf{x}\,, \tag{14}$$

the $3N \times 1$ vector $\mathbf{a}$ contains three $N \times 1$ subvectors corresponding to the three components of the optimized signals

$$\mathbf{a}_k = \begin{pmatrix} a_k^1\\ a_k^2\\ .\\ .\\ a_k^N\end{pmatrix}, \tag{15}$$

and the $3N \times 1$ vector $\mathbf{d}$ contains three $N \times 1$ subvectors corresponding to the three components of the recorded data

$$\mathbf{d}_k = \begin{pmatrix} d_k^1\\ d_k^2\\ .\\ .\\ d_k^N\end{pmatrix}. \tag{16}$$

Note that in eq. (14), the integration variable $\mathbf{x}$ represents the subsurface points within W, and that a summation is carried out over the index r.

The significance of eq. (12) is that $\boldsymbol{\Gamma}$ on the left-hand side of eq. (12) can be computed (based on eq. 14) as long as the medium is known and an estimate of the source location is available. The right-hand side of eq. (12) depends only on the recorded data, meaning that all the information the method requires about the unknown source is available and encoded within the data. Therefore, eq. (12) can be solved for $\mathbf{a}(\omega)$.

Even if only a subset of the data components are available, the formalism presented above is still valid and applicable. This is because eq. (13) can be readily modified to form a new system that corresponds to the available data components. As an example, eq. (13) can be modified for application in 2-D as

$$\underbrace{\overset{2N\times 2N}{\begin{pmatrix}\boldsymbol{\Gamma}_{11} & \boldsymbol{\Gamma}_{12}\\ \boldsymbol{\Gamma}_{21} & \boldsymbol{\Gamma}_{22}\end{pmatrix}}}_{\boldsymbol{\Gamma}} \underbrace{\overset{2N\times 1}{\begin{pmatrix}\mathbf{a}_1\\ \mathbf{a}_2\end{pmatrix}}}_{\mathbf{a}} = e^{i\omega T} \underbrace{\overset{2N\times 1}{\begin{pmatrix}\mathbf{d}_1\\ \mathbf{d}_2\end{pmatrix}^{*}}}_{\mathbf{d}^{*}}, \tag{17}$$

where $\boldsymbol{\Gamma}_{kl}$, $\mathbf{a}_k$ and $\mathbf{d}_k$ are defined by eqs (14)–(16), respectively. Similarly, eq. (13) can be modified for 3-D cases where only a subset of data (e.g. only vertical components) is available for all or some receivers.

After solving eq. (12) and finding $\mathbf{a}(\omega)$ for all frequencies, we can compute the optimal time-domain signals $\mathbf{a}^i(t)$ with an inverse Fourier transform. To image the source, these optimized signals must be injected by the receivers and the resulting wavefield $\boldsymbol{\psi}(\mathbf{x}, t)$ within the optimization window W must be scanned for the image of the source.

We started our argument by assuming that there is only one point source inside the medium. However, as we show in Appendix B, this argument can be generalized to hold true for any arbitrary extended (distributed) source. This is a result of the linearity of the problem and that a distributed source can be regarded as a collection of point sources. In other words, our method can be used for imaging a source regardless of it being a point source or not.

It is worth pointing out that computing $\boldsymbol{\Gamma}$ requires simulating the wave propagation to model the Green tensor for each receiver location. However, for a fixed configuration of receivers, $\boldsymbol{\Gamma}$ has to be computed only once. (Recall that $\boldsymbol{\Gamma}$ on the left-hand side of eq. (12) depends only on the receiver geometry and the properties of the medium and the right-hand side depends only on the recorded data.) Therefore, once $\boldsymbol{\Gamma}$ is computed and stored, we can reuse it to solve eq. (12) whenever a new source occurs within W. This means that for receivers with a fixed geometry, using our technique to image multiple sources can be computationally very efficient. One important aspect of the proposed source-imaging algorithm is that it can be simplified and applied for source imaging in acoustic media as well. We show in Appendix C that in acoustic media the method boils down to solving a linear system of equations with data on the right-hand side similar to eq. (12).

2.3 Relation to other techniques

The source-imaging algorithm formulated in Section 2 is an optimization method that is based on minimizing the objective function (4). For this reason, in the rest of this paper, to distinguishing our method from other techniques, we refer to it as the Optimal Source Imaging (OSI) method. In this section, we discuss how OSI is related to other common techniques for source imaging or wave focusing such as TR and the inverse filter method.

To see the connection between OSI and TR, let us first examine the structure of $\boldsymbol{\Gamma}$ and discuss the significance of its nine submatrices (shown in eq. 13) and the role they play in the optimization process. All elements of $\boldsymbol{\Gamma}$ hold information about the configuration of the focusing experiment, i.e. the relative positions of the receiver stations with respect to the inhomogeneities in the propagation medium and the focusing target. The role of the submatrix $\boldsymbol{\Gamma}_{kl}$ can be described as determining how the signal injected by the kth component of each receiver must be adjusted with respect to the signals emitted by the lth components of the other receivers in order to optimally reconstruct the source displacement field. $\boldsymbol{\Gamma}$ as defined by eq. (14) is in general a dense matrix. Approximating $\boldsymbol{\Gamma}$ in eq. (12) by the identity matrix I gives

$$\mathbf{a}(\omega) = \mathrm{e}^{i\omega T}\mathbf{d}^{*}(\omega). \tag{18}$$

The complex conjugation and multiplication of $\mathbf{d}(\omega)$ in eq. (18) by $\mathrm{e}^{i\omega T}$ amounts to TR of the data $\mathbf{d}(t)$ in the time domain. In other words, using the identity matrix as the most simplistic approximation for $\boldsymbol{\Gamma}$ in eq. (12) results in a new system of equations (as in eq. 18) that describes exactly the same process as TR. By replacing $\boldsymbol{\Gamma}$ with the identity matrix, we turn off the function of the submatrices of $\boldsymbol{\Gamma}$. This amounts to ignoring the interplay (cross-talk) between the components of the stations and make them work independently from one another to inject the time-reversed data. Therefore, we might say that TR is a special case of the more-general OSI with a crude approximation of $\boldsymbol{\Gamma}$ as the identity matrix.

OSI is also related to the inverse filtering (IF) method introduced by Tanter *et al.* (2000, 2001). For a concise summary of IF see Gallot *et al.* (2012). IF is a technique for calculating the optimal set of signals to be injected by a phased array in order to focus waves on a control point in inhomogeneous media. The method is

based on the matrix formalism of the propagation operator between a set of sources and control points that accounts for all of the propagation effects at a given frequency. In this sense, IF and OSI are not fundamentally different as both methods optimally focus energy in a limited region of space that is represented by, a set of control points in IF, and the area W in OSI. In IF, the Green functions required to form the propagator matrix are experimentally acquired using receivers near the control points and therefore knowledge of the medium is not needed. In OSI, these Green functions are numerically computed and therefore the medium must be known.

To calculate the optimal signals, Tanter *et al.* (2001) require the injected wavefield to collapse on a chosen control point as a monopole field that is impulsive in time. This is achieved through choosing an objective vector that is zero everywhere within the target region (vector of control points) except for the control point at the focusing target. Using this objective vector is essentially equivalent to the deltaness criterion originally used by Backus & Gilbert (1968) or a special case of the objective function 4 for an impulsive monopole source. In OSI, the injected wavefield is required to collapse onto the original source and this can be achieved without knowing the source in space or time and the source can have any mechanism. This is an essential element in OSI that is absent in IF method.

The relationship between TR, hybrid back propagation source-imaging techniques, and classical linear inverse solutions has been studied by several authors. For instance, Fukahata *et al.* (2014) show that, with certain assumptions, TR is approximately equivalent to a damped least squares solution with a large damping parameter. More recently, Nakahara & Haney (2015) use the concept of point spread function (PSF) to clarify the relation between TR and least-squares solutions and also to study their resolutions. It is important to point out that Γ^{OSI} defined by eq. (14) (or eq. C9 in the acoustic case) is not the same as Γ^{PSF} defined as the PSF by eq. (4) in Nakahara & Haney (2015). A comparison of the two definitions reveals that in Γ^{OSI} the continuous integration variable $\mathbf{x}$ is in the model space (subsurface locations limited within W), whereas in Γ^{PSF}, the integration variable $\mathbf{x}$ is in the data space (receiver locations). Γ^{OSI} therefore has a different meaning compared to Γ^{PSF} and the source image obtained by OSI is not readily comparable with the least squares solutions considered in Nakahara & Haney (2015) and Fukahata *et al.* (2014). To be more specific, recall that in OSI the source image is obtained by solving eq. (12) for optimal signals $\mathbf{a}$ and back propagating them. In this context, rather than the least squares solution, the OSI solution to the source-imaging problem is more closely related to a minimum length solution. In practice (see Section 4.3), a stable inversion of eq. (12) involves some sort of regularization in which case the OSI source image would correspond to a damped minimum length solution. The damped minimum length solution, however, can itself be related to the damped least squares solution. A detailed comparison between damped least squares and damped minimum length solutions and the way they are related, can be found in Menke (2012) or Snieder & Trampert (1999).

3 NUMERICAL EXPERIMENT

We apply the OSI method in a 2-D synthetic experiment to image a point source with a double-couple mechanism and compare the result with the same image produced by TR. The configuration of the experiment is shown in Fig. 1. The six diamonds represent the multi-component receivers, the white dot depicts the source location, and the white circle shows the optimization window W, used in the definition of the objective function in eq. (4). All receivers are at the surface ($z = 0$ m) with the first receiver at $\mathbf{x}^1(x, z) = (630\ \mathrm{m}, 0\ \mathrm{m})$ and the sixth receiver at $\mathbf{x}^6(x, z) = (1110\ \mathrm{m}, 0\ \mathrm{m})$. Adjacent receivers are 90 m apart. The earth model used for wave propagation is a heterogeneous elastic 2-D model with absorbing boundaries (Fig. 1) consisting of three layers. Wave propagation is simulated using an explicit finite-difference approximation of the 2-D elastic isotropic wave equation with an absorbing boundary condition on a 200 × 201 grid with grid spacings $dx = dz = 6$ m and with time step $dt = 1$ ms.

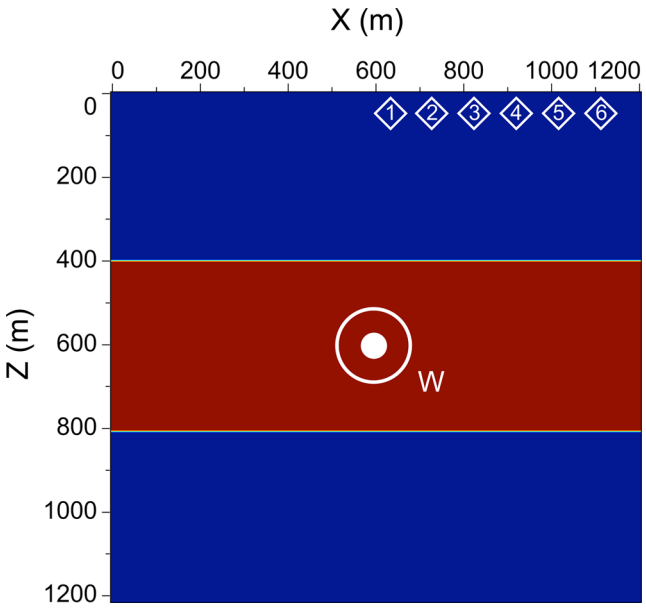

Figure 1. The elastic model and the configuration of the numerical experiments discussed in the text. The white diamonds show the location of the stations, the white circle W depicts a small subset of the medium that contains the focusing target which is represented by the white dot. The blue background colour represents $v_p = 3000\ \mathrm{m\,s^{-1}}$, $v_s = 2000\ \mathrm{m\,s^{-1}}$ and $\rho = 2000\ \mathrm{kg\,m^{-3}}$. The red background colour represents $v_p = 3750\ \mathrm{m\,s^{-1}}$, $v_s = 2500\ \mathrm{m\,s^{-1}}$ and $\rho = 3000\ \mathrm{kg\,m^{-3}}$.

The data vector $\mathbf{d}(t)$ is simulated using a localized double couple source with the slip in x-direction and the normal vector to fault in the z-direction located at $\boldsymbol{\xi} = (600\ \mathrm{m}, 600\ \mathrm{m})$ within W. The time dependence of the source is given by a Ricker wavelet with peak frequency of 55 Hz and peak time $t = 100$ ms. The dominant local P and S wavelengths at the source region are 68 and 45 m, respectively. We sample the displacement field generated by this source by the six receivers as time signals $d_n^i(t)$, $\forall i \in \{1, 2, \ldots, 6\}$, $\forall n \in \{1, 2\}$, and for $0\ \mathrm{s} < t < T = 0.6$ s. After simulating the data, we pretend that we do not know the exact location, time, and mechanism of the source. However, we assume that an estimate of the source location is available. This estimate is needed for defining the integration window W such that it contains the source. Here, W is a circular area with radius of 90 m. The integrand in eq. (14) is an oscillatory function, therefore to avoid dominant contribution from the end points, we apply a Gaussian taper to the edges of integration window W.

To form the matrix $\boldsymbol{\Gamma}$, in eq. (17), we require the Green tensors $\mathbf{G}(\mathbf{x}, t; \mathbf{x}^i, 0)$ for all receivers. We approximate the components of each Green tensor by injecting a band limited spike with frequencies between 2 and 140 Hz at each receiver location $\mathbf{x}^i$ and propagating the wavefield for $T = 0.6$ s. These wavefields are then Fourier transformed to the frequency domain and used in eq. (14) to compute the

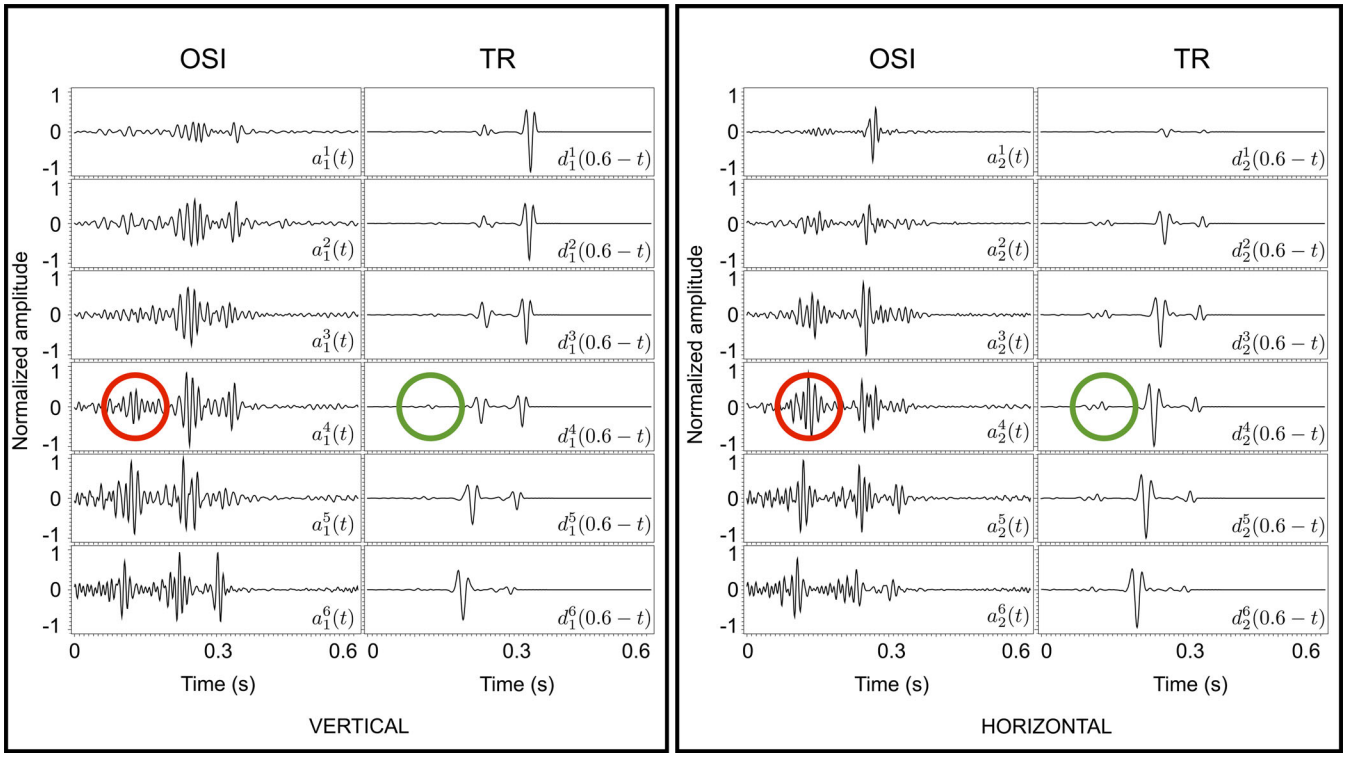

Figure 2. Vertical component of the optimal signals versus the timer-reversed vertical component of the data (left panel), and horizontal component of the optimal signals versus the time-reversed horizontal component of the data (right panel). The weak reflection energies (green circles) are amplified in the optimized signals (red circles).

elements of the 12×12 matrix $\mathbf{\Gamma}$ independently for all frequencies within the bandwidth of the experiment.

At this point, we can form the system of equations (17) for each frequency independently and solve the system for $\mathbf{a}^i(\omega)$, the Fourier coefficients of the optimized signals $\mathbf{a}^i(t)$. These optimized signals are then broadcast by the receivers to generate the injected displacement field $\boldsymbol{\psi}(\mathbf{x}, t)$ that optimally approximates the time-reversed source displacement field $\mathbf{u}(\mathbf{x}, T-t)$ and focuses at the correct source location within the optimization window W. Note that, in this 2-D example, $\boldsymbol{\psi}$ is a vector field with two components, a vertical and a horizontal component. The last step is to inspect (scan) the injected back-propagated wavefield $\boldsymbol{\psi}(\mathbf{x}, t)$ to detect the moment in time when the field is most concentrated. We identify this moment as the source time and the associated timeslice of $\boldsymbol{\psi}(\mathbf{x}, t)$ as the source image. After detecting the source image, the spatio-temporal characteristics of the source can be inferred from that image. Possible criteria to detect the source time can include high energy or a particular type of radiation pattern which is expected for the source. For example, a seismic source with a double-couple mechanism has a characteristic four-lobe radiation pattern for the *P*-wave (radial displacement) component (Aki & Richards 2002). The *P* and *S* components of the displacement field can be readily computed as the divergence and curl of the displacement field, respectively (Larmat *et al.* 2009). For the examples shown in this paper, we used the maximum energy criterion to detect the source location and time.

Figs 2 and 3 summarize the results of the numerical experiment described above. Fig. 2 consists of two panels. The left panel depicts the vertical component of the optimal signals in the column labelled OSI, and the vertical component of the time-reversed data in the column labelled TR. Similarly, the right panel depicts the horizontal component of the optimal signals in the column labelled OSI, and the horizontal component of the time-reversed data in the column labelled TR. The signals in each column (of both panels) have been normalized by dividing all samples by the maximum absolute value of the amplitude of all traces in the same column.

The optimization process has produced signals that are different from their corresponding time-reversed data in both amplitude and shape. For example, the small amplitude events in the time-reversed traces (e.g. the energy encircled in green) correspond to reflected energy from the discontinuity at $z = 800$ m in Fig. 1. Note how the same reflected events (i.e. the energy encircled in red) are amplified by OSI in the optimally computed signals.

Figs 3(a) and (b) depict the divergence (radial component or *P*-wave) and curl (transverse component or *S* wave) of the source displacement field enclosed within W at the activation time of the double-couple point source. We can think of Fig. 3(a) as the exact (true) *P*-wave image and of Fig. 3(b) as the exact (true) *S*-wave image of the source wavefield. The radial and transverse component of the optimally reconstructed time-reversed source displacement field $\boldsymbol{\psi}(\mathbf{x}, t)$ at the time of focus are shown in Figs 3(c) and (d), respectively. These are the *P*- and *S*-wave images of the source obtained by taking the divergence and curl, respectively, of $\boldsymbol{\psi}(\mathbf{x}, t)$. Finally, the *P*- and *S*-wave images of the source produced by TR are depicted in Figs 3(e) and (f), respectively. The OSI images (second row of Fig. 3) are superior to the TR images (third row). Note how the four lobes of the *P*-wave radiation pattern are resolved by OSI in Fig. 3(c), whereas it is impossible to recognize them in the corresponding TR image in Fig. 3(e). The four-lobe *S*-wave radiation pattern is not resolved by either OSI or TR. This is due to the source-receiver configuration in this experiment and the slip direction of the source and the way it radiates *S*-wave energy

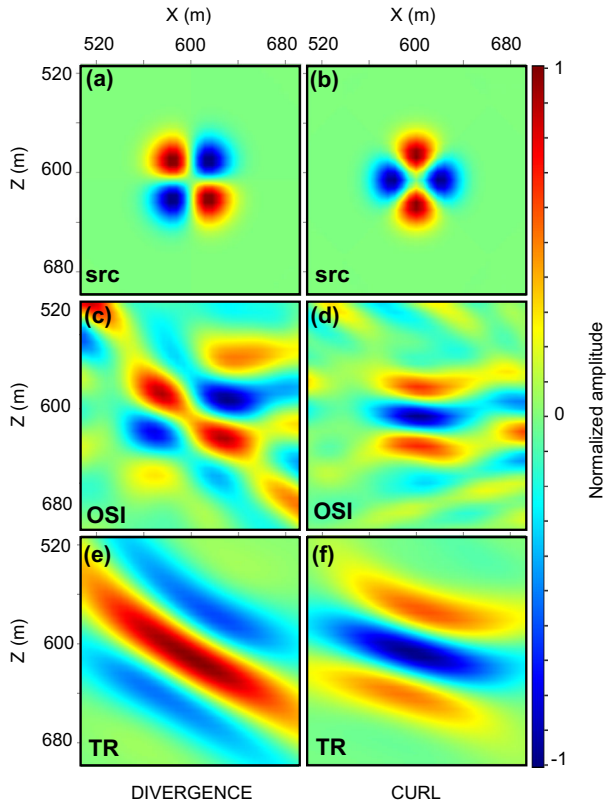

Figure 3. Divergence (a) and curl (b) components of the source displacement field enclosed within W at the activation time of the source are compared with the P-wave (c) and S-wave (d) images of the source produced by OSI, and with the P-wave (e) and S-wave (f) images of the source produced by TR.

(see Section 4.4 for another example and a more detailed discussion of this issue). Nevertheless, compared to the TR image (Fig. 3f), the OSI image (Fig. 3d) resembles the exact S-wave image (Fig. 3b) more closely in both size and orientation.

The improvement of the resolution in the OSI images, can be attributed to a more balanced illumination of the target. This is made possible by using the amplified reflected events in the optimized signals shown in Fig. 2. When the optimized signals are propagated, a strong coherent burst of energy is created by these amplified events. This coherent energy travels in advance of the direct arrival energy and part of it, after bouncing off the reflector at $z = 800$ m, illuminates the target from underneath. Of course, OSI did not create this energy out of nowhere. The energy is also present in the TR experiment, but it is much weaker. The observed improvement is mostly the result of detecting this weak energy by OSI and properly amplifying it in order to balance the illumination of the target. Effectively, this is equivalent of using the reflector at $z = 800$ m as an elastic mirror in order to augment the illumination angles, which, in the case of TR, are limited to the small angle subtended by the first and the last receivers.

4 SENSITIVITY TESTS AND ANALYSES

The success of the OSI method in producing accurate source images depends on the validity of the assumptions that were made in formulating the method. The most significant of these assumptions are knowledge of the elastic medium (e.g. P- and S-wave velocities and density) and an approximate location of the source. In this section, using elastic source-imaging simulations, we analyse the sensitivity of the OSI method to errors in the earth model and noise in data. We also study how the source image obtained by the method is affected by the size of the optimization window W which is determined by the size of the monitored region. Finally, we examine the resolution of the OSI method using synthetic tests with various source-receiver configurations.

For the first series of tests, we use the source-receiver configuration and the three-layer elastic earth model shown in Fig. 1. We simulate the data using an isotropic point source located at the white dot in Fig. 1. The time dependence of the source is given by a Ricker wavelet with peak frequency of 55 Hz and peak time at $t = 100$ ms. The true P-wave image of this isotropic point source is shown in Fig. 4(a). Here, by true P-wave image, we mean the image that one would obtain in a full-aperture diffraction-limited TR experiment by computing the divergence of the back-propagated displacement field at the time of focus. The true image therefore represents the diffraction-limited TR image of the point source for a perfect aperture (receivers placed equidistantly at a spacing of 60 m along the boundary of the computational domain in Fig. 1). The reason for not showing the S-wave image of the source in Fig. 4 is that the isotropic point source in this experiment does not generate S-waves at its activation time. Before carrying out the sensitivity tests, we use the simulated data (with no added noise) to image the source using the TR method with the source-receiver configuration and the earth model of Fig. 1 (henceforth the true earth model). Fig. 4(b) shows the resulting TR image of the source.

Fig. 4(c) shows the image of the source obtained using the OSI method with the true velocity model and with circular W of radius 90 m. The scalar quantity Q shown in this figure is a measure of precision of the image of the point source and is defined as

$$Q(I) = \frac{\int_W |\mathbf{x} - \boldsymbol{\xi}'|\, I^2(\mathbf{x})\, d\mathbf{x}}{\int_W I^2(\mathbf{x})\, d\mathbf{x}}, \tag{19}$$

where $I(\mathbf{x})$ denotes the value of the source image I at location $\mathbf{x}$, and $\boldsymbol{\xi}'$ is the detected source location defined as

$$\boldsymbol{\xi}' = \underset{\mathbf{x}\in W}{\operatorname{argmax}}\ |I(\mathbf{x})|. \tag{20}$$

The function $Q(I)$ gives a quantitative measure of the spread of energy around a detected point of maximum amplitude $\boldsymbol{\xi}'$ within the image I; the smaller Q is, the more focused and localized is the image.

Next, we repeat this source-imaging test using the OSI method applied partially by zeroing out the off-diagonal elements in each submatrix of $\boldsymbol{\Gamma}$ in eq. (17). This amounts to forcing OSI to optimize the injected signals using the components within each receiver independently of the other receivers and hence, ignoring the interplay of the receiver components among different stations. The source image obtained by this experiment is shown in Fig. 4(d). A comparison of the images shown in Figs 4(b)–(d) demonstrates that the OSI method, compared to TR, produces more focused images. It also indicates that to be most effective, the OSI optimization process must take the interplay among the components of different receivers into account. We next analyse the sensitivity of the OSI method to inaccuracies in the earth model.

4.1 Model

A method for solving the wave equation and a model that accurately describes the propagation medium are essential elements of the OSI

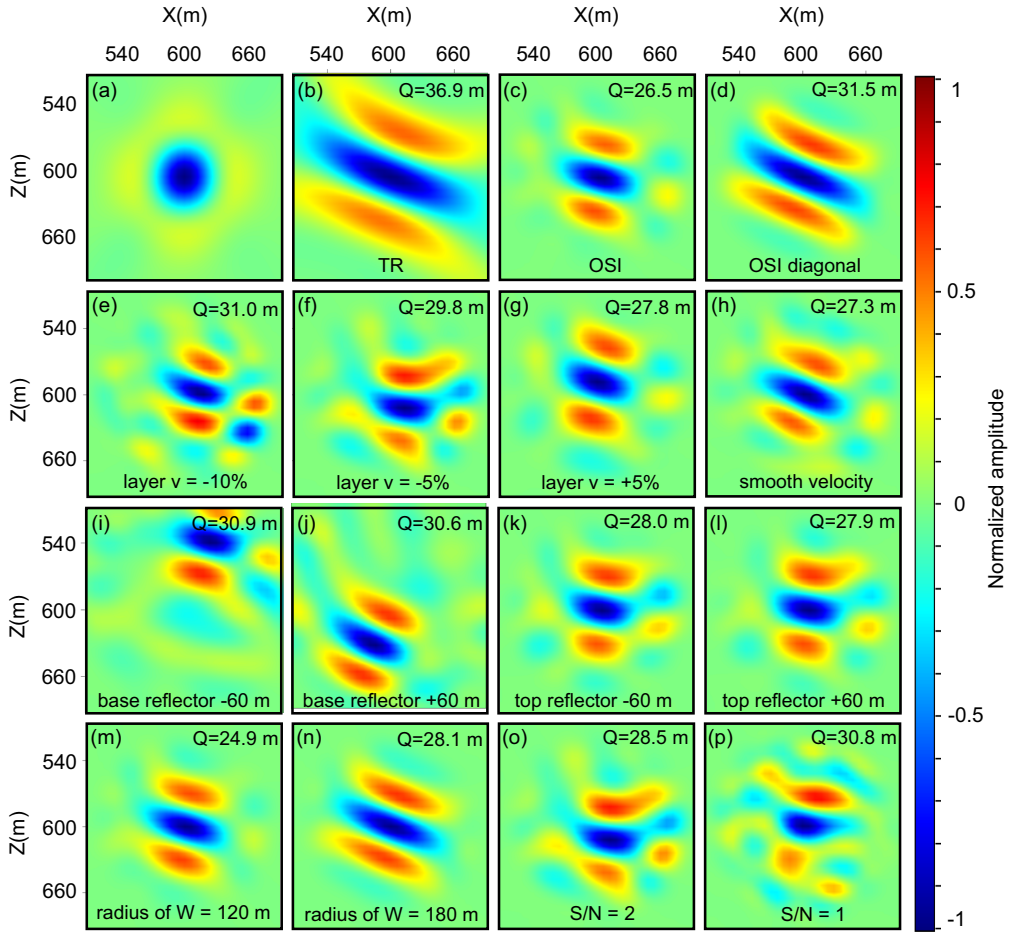

Figure 4. *P*-wave images of the point source associated with the source–receiver configuration depicted in figure showing (a) the true *P*-wave image of the isotropic point source, (b) TR image using true velocity, (c) OSI image using true velocity and optimization window with radius 90 m, (d) OSI image where OSI is applied partially such that the interplay between receiver components among different stations is ignored, (e) OSI image using a perturbed model where the density and velocities of the middle layer are decreased by 10 per cent, (f) OSI image using a perturbed model where the density and velocities of the middle layer are decreased by 5 per cent, (g) OSI image using a perturbed model where the density and velocities of the middle layer are increased by 5 per cent, (h) OSI image using a perturbed model by smoothing the true velocity with a Gaussian filter, (i) OSI image using a perturbed model where the width of the middle layer is altered by lowering its base interface by 60 m, (j) by raising its base interface by 60 m, (k) by lowering its top interface by 60 m, and (l) by raising its top interface by 60 m, (m) OSI image using the true velocity and optimization window W with radius 120 m, (n) OSI image using the true velocity and optimization window W with radius 180 m, (o) OSI image using the true velocity and data contaminated by noise with S/N = 2 and (o) OSI image using the true velocity and data contaminated by noise with S/N = 1. All images are obtained by computing the divergence of the injected wavefield at the time of focus.

method. These are required for estimating the Green tensors used for computing the optimal signals and also for back propagating those signals. Recall that the OSI method utilizes the reflected waves in the data to augment the incomplete acquisition (see Section 3). It is, therefore, important that the earth model used to compute the Green tensors contains the major reflectors in the medium with correct reflective strengths in their correct positions. More generally, the model must be accurate enough to correctly account for the scattered waves recorded in the data. This means that the model must ideally include all the impedance anomalies that could scatter the source energy back towards the receivers, that is, the impedance anomalies that are comparable in size to the dominant wavelengths in the experiment. In practice, an earth model with such an accuracy is not always available and the model used for source imaging contains errors.

In any source-imaging method, errors in the velocity model can cause the source image to be created at a wrong location or time. OSI is not an exception in this regard. Here we test the effect of using an erroneous earth model in the OSI method. By erroneous, we mean an earth model that is perturbed and somehow different compared to the true earth model (the model that was used to simulate data).

We first perturb the earth model by changing the density, and the *P*- and *S*-wave velocities of the middle layer in Fig. 1 by a fixed amount. Figs 4(e)–(g) show the *P*-wave images of the source as obtained in such tests where the perturbed earth model is constructed by changing the density and velocities of the middle layer by -10 per cent, -5 per cent, and $+5$ per cent, respectively. The time and location of the focus (source image) in these tests are detected automatically using the maximum energy criterion defined by eq. (19).

To test the sensitivity of the method to inaccuracies in the reflection coefficient of the reflectors, we perturb the earth model by smoothing it with a Gaussian smoothing filter with standard width

of 12 m. Smoothing the earth model decreases the impedance contrast across the reflecting interfaces and leads to weaker reflected energy from the interfaces in the model. (For example, after smoothing, the PP reflected amplitude recorded by the vertical component of receiver 1 in Fig. 1 decreases about 80 per cent.) The *P*-wave source image obtained by OSI using this smoothed velocity model is shown in Fig. 4(h). More severe smoothing of the earth model leads to more degradation of the focus quality.

Next, we perturb the earth model by changing the depth of the interfaces in the true model. Figs 4(i) and (j) are source images obtained by OSI using models that are perturbed by lowering and raising the base reflector of the middle layer in Fig. 1 by -60 and $+60$ m, respectively. Figs 4(k) and (l) show the result of similar tests for perturbations in the depth of the top interface of the middle layer by -60 and $+60$ m, respectively.

As implied by the Q measure associated with source images in Figs 4(e)–(l), the quality of the focus deteriorates as a result of error in the earth model, however, the OSI images obtained with the perturbed earth models in these examples are still more focused than the TR image (Fig. 4b). Note that error in the earth model can cause the image to focus at a wrong location, (e.g. see Fig. 4i). It is important that this error in the location of the source is not larger than the extent of the optimization window W.

Repeating the experiments shown in Figs 4(e)–(l) with the TR method indicates that TR is less sensitive than OSI to perturbations in the earth model; the resulting source images (not shown here) show little or no significant changes compared to the TR image in Fig. 4(b). This observation can be explained by noting that TR does not require the earth model for computing the back-propagating signals; the injected signals in TR are just the time reversed data and knowledge of the medium is only used for simulating the back-propagation step. In OSI however, knowledge of the medium is used in computation of the optimal signals and also in the back-propagation step.

4.2 The optimization window

The optimization area W in OSI source imaging is defined as the area that is known to contain the source. The position of W can be chosen based on some *a priori* information or estimate about the source location (e.g. using more-conventional inversion-based source location techniques). The size of W must be chosen based on the amount of certainty in the estimate of source location such that we can be certain that the source is somewhere within W. To test how the OSI source image is affected by the size of W, we repeat the OSI imaging of the point source that was shown in Fig. 4(c) but with larger sizes of W. Figs 4(m) and (n) show the OSI images obtained by these experiments wherein the radius of W is chosen to be 120 and 180 m, respectively. It is evident by these tests that the source image obtained by OSI depends on the size of W. This is because W is used directly in the definition of the objective function (4) upon which we based the formulation of the OSI method. With a limited number of receivers and illumination angles, the smaller W (the smaller the uncertainty in the location of the source) is, the easier it is to minimize the OSI objective function over W and the more effective OSI is. However, there is a lower limit on how small W can be to obtain best imaging results. More tests like the ones shown above indicate that the best focusing results are obtained when the radius of the circular window defining W is about two to three times the dominant wavelength in the experiment.

4.3 Noise

Applying the OSI method for source imaging hinges upon the validity of eq. (2) which allows us to form and solve the system of equations (12) without explicit knowledge of the source location, time, and mechanism. In a real source-imaging scenario, data is contaminated with noise and, therefore, eq. (12) must be modified as

$$\mathbf{\Gamma}(\omega)\,\mathbf{a}(\omega) \approx \mathbf{e}^{i\omega T}(\mathbf{d}^*(\omega) + \boldsymbol{\eta}^*(\omega)), \tag{21}$$

with $\boldsymbol{\eta}$ denoting the noise vector and $\mathbf{d}$ the noise free data described by eq. (2).

The stability of the solution $\mathbf{a}$ to eq. (21) depends on the condition number of the matrix $\mathbf{\Gamma}(\omega)$, which itself depends on the configuration of the receivers, the properties of the medium, and the frequency for which the $\mathbf{\Gamma}(\omega)$ is computed. If $\mathbf{\Gamma}(\omega)$ is ill-conditioned, a regularization technique, e.g. truncated SVD can be used to find a stable solution to eq. (21).

To see how the presence of noise in data can affect the OSI method, we contaminated the simulated data with uncorrelated band-limited Gaussian random noise with the same bandwidth as data and with signal to noise ratio of 2. Here the signal to noise ratio is defined as rms amplitude of signal (simulated data) to rms amplitude of the random noise. (If the data is contaminated with correlated noise, e.g. energy from a different source outside the optimization window, then the data must be processed in order to suppress the correlated noise, or if possible, the optimization window must be chosen large enough to contain the secondary source of energy.)

We then used the OSI method (with true velocity) to image the source using this noisy data. For the configuration of this example, the condition number of $\mathbf{\Gamma}(\omega)$ varies between about 1.4×10^6 at 10 Hz to about 20 at 130 Hz, that is, $\mathbf{\Gamma}$ is ill-conditioned at low frequencies. (The reason why the condition number of $\mathbf{\Gamma}$ is larger for low frequencies can be explained by a thought experiment: consider a situation where two receivers are coincident, that is, $\mathbf{x}^i = \mathbf{x}^j$ in the definition of the $\mathbf{\Gamma}$ in eq. (14). In that case, $\mathbf{\Gamma}$ becomes singular as two of its rows and columns are identical. This corresponds to a zero singular value in the spectrum of $\mathbf{\Gamma}$. Now suppose that the two receivers are very close but not exactly coincident. In this situation, for low frequencies (large wavelengths) the two receivers would record almost the same signals which means two rows and columns of $\mathbf{\Gamma}$ are close but not quite the same. As a result $\mathbf{\Gamma}$ becomes nearly singular which corresponds to a small singular value in the spectrum.) To regularize the problem, we use TSVD to lower the condition number of the $\mathbf{\Gamma}$ matrices below a constant threshold of 50 for all frequencies. The *P*-wave source image obtained by this experiment is shown in Fig. 4(o).

Finally, we repeat this experiment with stronger noise with signal to noise ratio of 1. The *P*-wave source image obtained by this experiment is shown in Fig. 4(p). These experiments show that the OSI method, if properly regularized, can tolerate the presence of noise in data. Other regularization techniques such as damped singular value decomposition yield similar results. To produce the source images in Figs 4(o) and (p), we have assumed the source time (the time of focus) to be known. This assumption is only necessary because the maximum energy at the focus is not always a sufficient criterion for detecting the source image in experiments with noisy data. A more sophisticated/intelligent method of scanning the injected wavefield for detecting the source can obviate the need for knowing the source time in such cases.

4.4 Configuration of the experiment

The effectiveness and resolution of a source-imaging method depends on the configuration of the experiment and the quality (adequacy) of the sampling of the source wavefeild by the receivers. This includes the location of the source relative to the receiver array, the geometry and spatial distribution of the receiver array, as well as the source function, mechanism and radiation pattern. For example, Tanter *et al.* (2001) show how focusing using an array of transducers depends on the eigenvalue spectrum of the propagation operator associated with a particular configuration of the transducers and the focusing target. Similarly in OSI, the number of significant eigenvalues of the $\mathbf{\Gamma}$ matrix for a given source and receiver configuration says something about the degrees of freedom in the acquisition geometry (see for instance the thought experiment in Section 4.3). The precise connection between the eigenvalue spectrum of $\mathbf{\Gamma}$ and the acquisition geometry is a topic of future investigation.

To demonstrate the dependence of the resolution of the source-imaging method on the configuration of the experiment, we compute the OSI and TR images associated with point sources (with isotropic radiation pattern) at the nine locations depicted by the white dots in Fig. 5(a). The OSI impulse responses and the corresponding

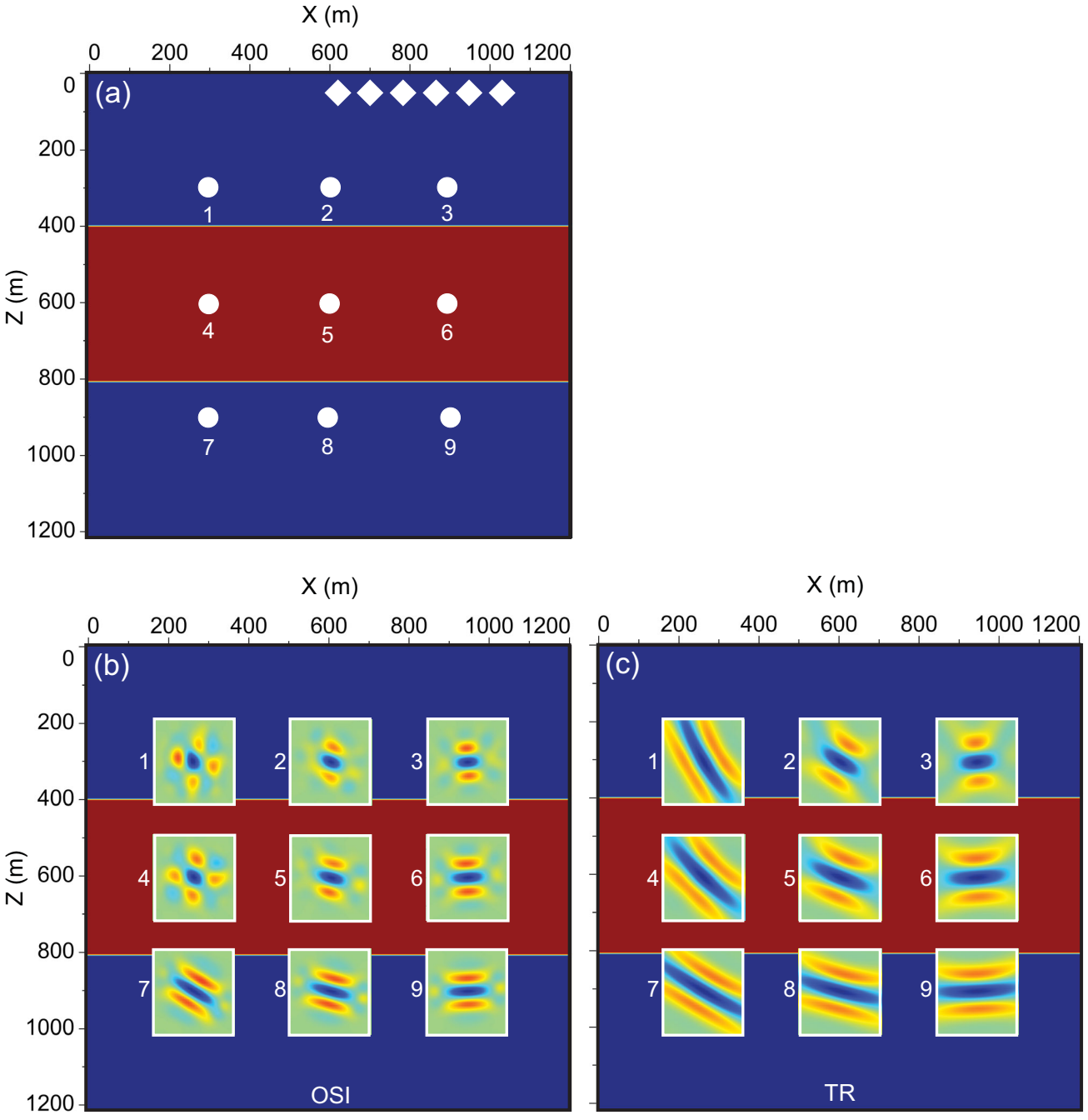

Figure 5. Resolution test for the linear receiver geometry. Panel (a) shows the configuration of the receivers (the diamonds) and the trial source locations (nine white dots). Panel (b) contains nine images which are impulse responses for nine OSI source-imaging experiments, imaging point sources at the white dots shown in panel (a). Panel (c) contains nine images which are impulse responses for nine TR source-imaging experiments, imaging point sources at the white dots shown in panel (a).

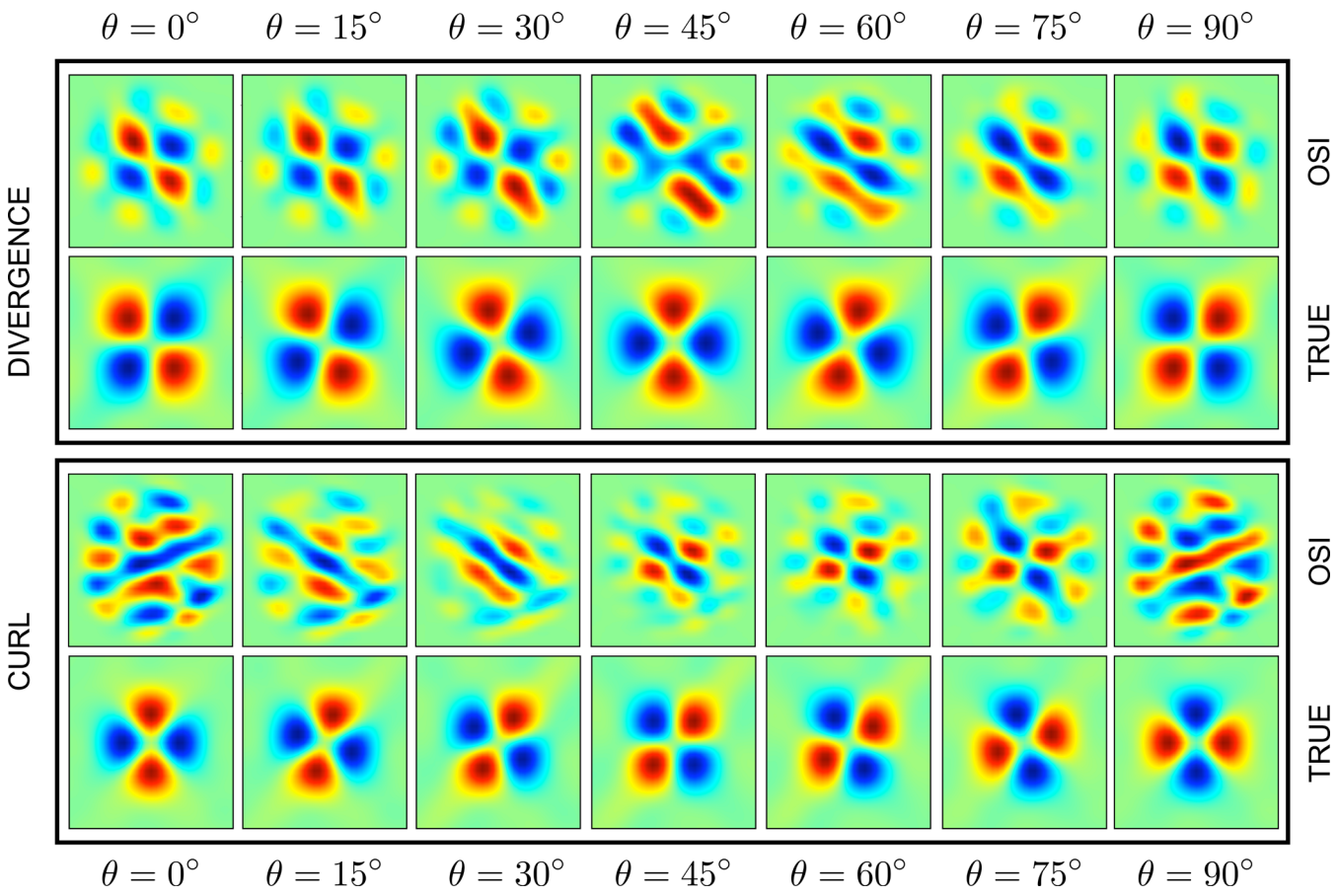

Figure 6. Imaging of a double-couple source with different orientations. The orientation of the source is specified by the angle θ measured relative to horizontal. The receiver geometry is the same as that shown in Fig. 4 and the source is at location 4. Top panel: the first row in the top panel shows the divergence of the OSI-optimized wavefield at the time of focus (the *P*-wave image) for different orientations of the double-couple source. The second row in the top panel depicts the true *P*-wave image of the double-couple source with different orientations of the source. Bottom panel: the first row in the bottom panel shows the curl of the OSI-optimized wavefield at the time of focus (the *S*-wave image) for different orientations of the double-couple source. The second row in the bottom panel depicts the true *S*-wave image of the double-couple source with different orientations of the source.

TR impulse responses are shown in Figs 5(b) and (c), respectively. As illustrated by these images, the resolution in both OSI and TR source-imaging experiments varies with location of the source and the way it is situated relative to the receivers and the reflecting interfaces in the earth model. Comparing Figs 5(b) and (c) shows that the resolution achievable by the OSI method is generally higher than that for TR. The noticeable improvement of the OSI resolution compared to the TR resolution, for example, in locations 1, 2, 4 and 5, is the result of augmentation of the illumination angles by the reflectors in the velocity model, but even below the lowest reflector the OSI images are more localized than the TR images.

Apart from the source-receiver configuration, the ability to properly image a source could also depend on the source radiation pattern and orientation of its nodal planes relative to the receiver array. To illustrate this point, we use the configuration shown in Fig. 5(a) and repeat the source-imaging experiment for a double-couple point source at source position 4. We start by a horizontal double-couple source with $\theta = 0$, where θ defines the orientation angle of the source slip direction measured with respect to horizontal. After imaging the double-couple source, we rotate its orientation by 15 degrees clockwise and image it again. We repeat this for $\theta = 0^\circ$, 15°, 30°, 45°, 60°, 75° and 90°. The OSI images obtained by this process are shown in Fig. 6. The top panel in Fig. 6 shows the divergence (*P* wave) and the bottom panel shows the curl (*S* wave) of the back-propagated displacement wavefield at the time of focus. The first row in each panel shows the images produced by the OSI method. The second row depicts the true images of the source and are included as reference. By true image, we mean the ideal *P*- or *S*-wave image of the source obtained by a diffraction-limited complete-aperture TR experiment.

Consider the OSI images in the divergence panel (top panel). At $\theta = 0^\circ$ the four-lobe *P*-wave radiation pattern of the source is well resolved. The quality of the *P*-wave image, however, degrades as θ increases to 45° and then it improves again from $\theta = 45^\circ$ to $\theta = 90^\circ$. Now, consider the OSI images in the curl panel (bottom panel). The quality of the *S*-wave image is poor initially at $\theta = 0^\circ$. It then improves as theta increases to 45°, and degrades again from $\theta = 45^\circ$ to $\theta = 90^\circ$. Note that in this 2-D example, regardless of the orientation of the source, the receivers record enough body-wave energy (*P* or *S* type) so the source mechanism and its orientations can be inferred from either *P*- or *S*-wave image or both. In a 3-D experiment, however, a double-couple source could be oriented in such a way that it radiates no body waves towards the receivers. (For instance, consider a case where the receivers are situated along the null axis of the body wave radiation pattern of a double-couple source.) In such a case, the direct arrival body wave energy of the source cannot be sensed in the data and therefore cannot be recovered by the imaging process.

The tests shown in this section are all 2-D examples. Seismic source imaging in 3-D is more challenging because adequate sampling of the source wavefield is much harder in 3-D than it is in 2-D. In addition, compared to 2-D, numerical modelling of 3-D wave propagation requires more computing resources. One way to deal with these problems is to image the seismic source using only the surface waves. As opposed to body waves, surface waves essentially propagate in 2-D. Therefore, a 3-D source-imaging experiment that just uses surface waves can be treated as a 2-D problem (e.g. Larmat *et al.* 2006). For proper imaging of deep earthquakes, however, it might be necessary to use body waves.

5 CONCLUSIONS

TR methods rely on the TR invariance of the wave operator. When acquisition is incomplete, source-imaging techniques based on the TR process are not optimal. In this paper, to overcome the limitations imposed by incomplete data acquisition, we approach source imaging as an optimization problem. This OSI approach provides a more general solution to seismic source imaging compared to TR. To apply OSI in source imaging, the medium must be known and also an estimate of the source position must be available. Apart from these two requirements, no other *a priori* information is needed by the method. For source imaging using receiver stations with a fixed geometry, the application of the method can be computationally efficient. Moreover, the method is applicable for source imaging in both elastic and acoustic media.

Using numerical examples simulating an elastic source-imaging experiment with sparse receiver geometry, we demonstrated that OSI can produce better resolved images of an unknown source compared to TR. We then discussed the main assumptions and requirements of the OSI method and analysed its sensitivity to errors in parameters such as the earth model used by the method for modelling wave propagation and the size of the optimization area. We also studied the effects of noise in data on the OSI image and showed that if properly regularized, the method can tolerate the presence of noise in data with $S/N \geq 1$. The efficacy of the method also depends on the configuration of the experiment and the radiation pattern of the source with respect to the receiver array.

One area of geophysics that is a good candidate for application of OSI is imaging earthquake sources. This is because of three reasons: The first reason is that a relatively reliable elastic model of the earth is available in global seismology which can be used by OSI. The second reason is that the advantages of OSI over TR are most pronounced in experiments with sparse (incomplete) acquisition geometry. The global network of seismometers does not have a uniform distribution on the Earth and therefore earthquakes that occur in certain areas cannot be recorded properly. And the third reason is that the data quality in terms of signal-to-noise ratio for the strong earthquakes recorded in global seismology is often good.

ACKNOWLEDGEMENTS

This research was supported by the sponsor companies of the Consortium Project on Seismic Inverse Methods for Complex Structures. We are thankful to Dr Jon Sheiman for supporting us with invaluable insights. The software used to produce the results in this paper was written in Java and Jython with the use of libraries in the Mines Java Toolkit freely available at https://github.com/dhale/jtk.

REFERENCES

Aki, K. & Richards, P., 2002. *Quantitative Seismology,* 2nd edn, University Science Books.

Anderson, B.E., Douma, J., Ulrich, T. & Snieder, R., 2015. Improving spatio-temporal focusing and source reconstruction through deconvolution, *Wave Motion,* **52,** 151–159.

Artman, B., Podladtchikov, I. & Witten, B., 2010. Source location using time-reverse imaging, *Geophys. Prospect.,* **58**(5), 861–873.

Aubry, J.-F., Tanter, M., Gerber, J., Thomas, J.-L. & Fink, M., 2001. Optimal focusing by spatio-temporal inverse filter. ii. experiments. application to focusing through absorbing and reverberating media, *J. acoust. Soc. Am.,* **110**(1), 48–58.

Backus, G. & Gilbert, F., 1968. The resolving power of gross earth data, *Geophys. J. Int.,* **16**(2), 169–205.

Baig, A. & Urbancic, T., 2010. Microseismic moment tensors: a path to understanding frac growth, *Leading Edge,* **29**(3), 320–324.

Blomgren, P., Papanicolaou, G. & Zhao, H., 2002. Super-resolution in time-reversal acoustics, *J. acoust. Soc. Am.,* **111**(1), 230–248.

Cassereau, D. & Fink, M., 1993. Focusing with plane time-reversal mirrors: an efficient alternative to closed cavities, *J. acoust. Soc. Am.,* **94**(4), 2373–2386.

Douma, J. & Snieder, R., 2015. Focusing of elastic waves for microseismic imaging, *Geophys. J. Int.,* **200,** 390–401.

Eaton, D.W. & Forouhideh, F., 2011. Solid angles and the impact of receiver-array geometry on microseismic moment-tensor inversion, *Geophysics,* **76**(6), WC77–WC85.

Eisner, L., Williams-Stroud, S., Hill, A., Duncan, P. & Thornton, M., 2010. Beyond the dots in the box: microseismicity-constrained fracture models for reservoir simulation, *Leading Edge,* **29**(3), 326–333.

Fink, M., 1997. Time reversed acoustics, *Phys. Today,* **50**(3), 34–40.

Fink, M., 2006. Time-reversal acoustics in complex environments, *Geophysics,* **71**(4), SI151–SI164.

Fink, M., 2008. Time-reversal waves and super resolution, *Journal of Physics: Conference Series,* **124,** 012004, doi:10.1088/1742-6596/124/1/012004.

Fukahata, Y., Yagi, Y. & Rivera, L., 2014. Theoretical relationship between back-projection imaging and classical linear inverse solutions, *Geophys. J. Int.,* **196**(1), 552–559.

Gallot, T., Catheline, S., Roux, P. & Campillo, M., 2012. A passive inverse filter for greens function retrieval, *J. acoust. Soc. Am.,* **131**(1), EL21–EL27.

Jost, M.u. & Herrmann, R., 1989. A students guide to and review of moment tensors, *Seismol. Res. Lett.,* **60**(2), 37–57.

Kawakatsu, H. & Montagner, J.-P., 2008. Time-reversal seismic-source imaging and moment-tensor inversion, *Geophys. J. Int.,* **175**(2), 686–688.

Kim, Y., Liu, Q. & Tromp, J., 2011. Adjoint centroid-moment tensor inversions, *Geophys. J. Int.,* **186**(1), 264–278.

Kuperman, W., Hodgkiss, W.S., Song, H.C., Akal, T., Ferla, C. & Jackson, D.R., 1998. Phase conjugation in the ocean: experimental demonstration of an acoustic time-reversal mirror, *J. acoust. Soc. Am.,* **103**(1), 25–40.

Larmat, C., Montagner, J.-P., Fink, M., Capdeville, Y., Tourin, A. & Clévédé, E., 2006. Time-reversal imaging of seismic sources and application to the great sumatra earthquake, *Geophys. Res. Lett.,* **33**(19), L19312, doi:10.1029/2006GL026336.

Larmat, C., Guyer, R. & Johnson, P., 2009. Tremor source location using time reversal: selecting the appropriate imaging field, *Geophys. Res. Lett.,* **36**(22), 22304, doi:10.1029/2009GL040099.

Larmat, C., Guyer, R.A. & Johnson, P.A., 2010. Time-reversal methods in geophysics, *Phys. Today,* **63**(8), 31–35.

Lu, R., Toksöz, M.N. & Willis, M.E., 2008. Locating microseismic events with time reversed acoustics: a synthetic case study, in *2008 SEG Annual Meeting,* pp. 1342–1346, Society of Exploration Geophysicists.

Maxwell, S.C. & Urbancic, T.I., 2001. The role of passive microseismic monitoring in the instrumented oil field, *Leading Edge,* **20**(6), 636–639.

McMechan, G.A., 1982. Determination of source parameters by wavefield extrapolation, *Geophys. J. Int.,* **71**(3), 613–628.

McMechan, G.A., Luetgert, J. & Mooney, W., 1985. Imaging of earthquake sources in Long Valley Caldera, California, 1983, *Bull. seism. Soc. Am.,* **75**(4), 1005–1020.
Menke, W., 2012. *Geophysical Data Analysis: Discrete Inverse Theory,* Academic Press.
Montaldo, G., Tanter, M. & Fink, M., 2003. Real time inverse filter focusing through iterative time reversal, *J. acoust. Soc. Am.,* **115,** 768–775.
Nakahara, H. & Haney, M.M., 2015. Point spread functions for earthquake source imaging: an interpretation based on seismic interferometry, *Geophys. J. Int.,* **202**(1), 54–61.
Robert, J.-L. & Fink, M., 2008. Greens function estimation in speckle using the decomposition of the time reversal operator: application to aberration correction in medical imaging, *J. acoust. Soc. Am.,* **123**(2), 866–877.
Schuster, G.T., Hanafy, S. & Huang, Y., 2012. Theory and feasibility tests for a seismic scanning tunnelling macroscope, *Geophys. J. Int.,* **190**(3), 1593–1606.
Shapiro, S.A., 2008. *Microseismicity: A Tool for Reservoir Characterization,* EAGE Publications.
Shearer, P.M., 2009. *Introduction to Seismology,* Cambridge Univ. Press.
Snieder, R., 2002. Time-reversal invariance and the relation between wave chaos and classical chaos, in *Imaging of Complex Media with Acoustic and Seismic Waves,* pp. 1–16, eds Fink, M., Kuperman, W.A., Montagner, J.-P. & Tourin, A., Springer.
Snieder, R. & Trampert, J., 1999. Inverse problems in geophysics, in *Wavefield Inversion,* pp. 119–190, ed. Wirgin, A., Springer.
Song, F. & Toksöz, M.N., 2011. Full-waveform based complete moment tensor inversion and source parameter estimation from downhole microseismic data for hydrofracture monitoring, *Geophysics,* **76**(6), WC103–WC116.
Stein, S. & Wysession, M., 2003. *An Introduction to Seismology, Earthquakes, and Earth Structure,* Blackwell Publishing.
Tanter, M., Thomas, J.-L. & Fink, M., 2000. Time reversal and the inverse filter, *J. acoust. Soc. Am.,* **108**(1), 223–234.
Tanter, M., Aubry, J., Gerber, J., Thomas, J. & Fink, M., 2001. Optimal focusing by spatio-temporal inverse filter. I. Basic principles, *J. acoust. Soc. Am.,* **110**(1), 37–47.
Tarantola, A., 2005. *Inverse Problem Theory and Methods for Model Parameter Estimation,* SIAM.
Vellekoop, I., Lagendijk, A. & Mosk, A., 2010. Exploiting disorder for perfect focusing, *Nature Photonics,* **4**(5), 320–322.
Wapenaar, K., Ruigrok, E., van der Neut, J. & Draganov, D., 2011. Improved surface-wave retrieval from ambient seismic noise by multi-dimensional deconvolution, *Geophys. Res. Lett.,* **38**(1), doi:10.1029/2010GL045523.
Wu, R.-S. & Ben-Menahem, A., 1985. The elastodynamic near field, *Geophys. J. Int.,* **81**(3), 609–621.
Zhu, T., 2014. Time-reverse modelling of acoustic wave propagation in attenuating media, *Geophys. J. Int.,* **197**(1), 1–12.

APPENDIX A: PARTICLE MOTION NEAR THE SOURCE

In Section 2.2, we assumed that in the near-source region the particle displacements are proportional to the source equivalent force. Here, we justify this assumption by studying the behaviour of the particle displacements in the region near a unidirectional point force.

Consider an elastic medium with a point force $\mathbf{f}(t)$ applied at the origin where the source region is assumed to be locally homogeneous. Then the displacement field $\mathbf{u}(\mathbf{x}, t)$ due to this point force is (Aki & Richards 2002)

$$u_i(\mathbf{x},t) = \frac{1}{4\pi\rho}\,(3\gamma_i\gamma_j - \delta_{ij})\,\frac{1}{r^3}\int_{r/\alpha}^{r/\beta}\tau\, f_j(t-\tau)\,\mathrm{d}\tau + \frac{1}{4\pi\rho\alpha^2}\,\gamma_i\gamma_j\,\frac{1}{r}\,f_j\left(t-\frac{r}{\alpha}\right) - \frac{1}{4\pi\rho\beta^2}\,(\gamma_i\gamma_j-\delta_{ij})\,\frac{1}{r}\,f_j\left(t-\frac{r}{\beta}\right), \tag{A1}$$

where $r = |\mathbf{x}|$ is the distance from the origin, $\gamma_i = x_i/r$ are the direction cosines, δ is the Dirac delta function, ρ is the density, α is the P-wave velocity, and β is the S-wave velocity with $\alpha > \beta$.

Using eq. (A1), we can calculate the limit

$$\lim_{r\to 0} 4\pi\rho r\, u_i(\mathbf{x},t) = \frac{1}{2}\left(\frac{1}{\alpha^2}+\frac{1}{\beta^2}\right)\delta_{ij}\, f_j(t) + \frac{1}{2}\left(\frac{1}{\beta^2}-\frac{1}{\alpha^2}\right)\gamma_i\gamma_j\, f_j(t). \tag{A2}$$

The expression on the right-hand side of eq. (A2) is called the Somigliana tensor (Aki & Richards 2002). In vector form, eq. (A2) is given by

$$\lim_{r\to 0} 4\pi\rho r\, \mathbf{u}(\mathbf{x},t) = \frac{1}{2}\left(\frac{1}{\alpha^2}+\frac{1}{\beta^2}\right)\mathbf{f}(t) + \frac{1}{2}\left(\frac{1}{\beta^2}-\frac{1}{\alpha^2}\right)\hat{\mathbf{r}}\,(\hat{\mathbf{r}}\cdot\mathbf{f}(t)), \tag{A3}$$

where $\hat{\mathbf{r}}_i = \gamma_i$.

When $\hat{\mathbf{r}} \parallel \mathbf{f}$, expression (A3) reduces to

$$\lim_{r\to 0} 4\pi\rho r\, \mathbf{u}(\mathbf{x},t) = \frac{1}{\beta^2}\,\mathbf{f}(t), \tag{A4}$$

and when $\hat{\mathbf{r}} \perp \mathbf{f}(t)$, expression (A3) reduces to

$$\lim_{r\to 0} 4\pi\rho r\, \mathbf{u}(\mathbf{x},t) = \frac{1}{2}\left(\frac{1}{\alpha^2}+\frac{1}{\beta^2}\right)\mathbf{f}(t). \tag{A5}$$

In both situations the displacement at the source location is parallel to the excitation. In other words, the force and the displacement are always in phase at the origin and no matter what $\mathbf{f}(t)$ is, eq. (6) holds true at the source location. This result is confirmed by Wu & Ben-Menahem (1985) who show (in fig. 2 of their paper) the motion of the elastodynamic field in the near-source region of a unidirectional force. Note that we apply eq. (6) only at the source position. One can see this in eq. (7) where the term that comes from eq. (6) contains a delta function. In other words, eq. (6) only gives a contribution at the source location, where it is exact.

APPENDIX B: OPTIMIZED IMAGING OF AN EXTENDED ELASTIC SOURCE

In Section 2.2, we formulated the OSI optimization for imaging a point source. Here, we show that this formulation is equally applicable for imaging any source (not just a point source) with arbitrary spatio-temporal characteristics.

We can model a distributed source as a succession of point sources that occur at locations $\boldsymbol{\xi}$, and with moment tensor $\mathbf{M}(\boldsymbol{\xi}, t)$ defined for $\boldsymbol{\xi} \in W$ and $t \in [0, T]$, and write

$$\mathbf{M}(\mathbf{x},t) = \int \mathbf{M}(\boldsymbol{\xi},t)\,\delta(\mathbf{x}-\boldsymbol{\xi})\,\mathrm{d}\boldsymbol{\xi}\,. \tag{B1}$$

The nth component of the data vector $\mathbf{d}(t)$ associated with this extended source and recorded by the station at $\mathbf{x}^i$ can be expressed as

$$d_n^i(t) = \int M_{pq}(\boldsymbol{\xi},t) * \frac{\partial G_{np}(\mathbf{x}^i,t;\boldsymbol{\xi},0)}{\partial\xi_q}\,\mathrm{d}\boldsymbol{\xi}, \tag{B2}$$

where $M_{pq}(\boldsymbol{\xi}, t)$ denotes the elements of the moment tensor $\mathbf{M}$ of the point source at $\boldsymbol{\xi}$, and G_{np} represents the elements of the elastodynamic Green tensor $\mathbf{G}$. In the frequency domain, eq. (B2) becomes

$$d_n^i(\omega) = \int M_{pq}(\boldsymbol{\xi},\omega)\,\frac{\partial G_{np}(\mathbf{x}^i;\boldsymbol{\xi},\omega)}{\partial\xi_q}\,\mathrm{d}\boldsymbol{\xi}. \tag{B3}$$

The body force equivalent of the distributed source can be written as (Aki & Richards 2002)

$$f_n(\mathbf{x}, t) = -\int M_{nq}(\boldsymbol{\xi}, t)\, \frac{\partial \delta(\mathbf{x}-\boldsymbol{\xi})}{\partial x_q}\, \mathrm{d}\boldsymbol{\xi} \tag{B4}$$

where δ represents the Dirac delta function.

With eqs (B3) and (B4) defining the data and the body force equivalent for the distributed source, we can repeat the same steps we took in Section 2 to formulate the optimization problem and obtain

$$a_p^j(\omega) \int_W G_{rn}^{i*} G_{rp}^j \, \mathrm{d}\mathbf{x} = \int \mathrm{e}^{i\omega T} M_{pq}^*(\boldsymbol{\xi}, \omega) \frac{\partial G_{np}^*(\mathbf{x}^i; \boldsymbol{\xi}, \omega)}{\partial \xi_q}\, \mathrm{d}\boldsymbol{\xi}, \tag{B5}$$

which can be simplified using (B3) as

$$a_p^j(\omega) \int_W G_{rn}^{i*}\, G_{rp}^j \, \mathrm{d}\mathbf{x} = \mathrm{e}^{i\omega T}\, d_n^{i*}. \tag{B6}$$

Eq. (B6) represents a system of equations that can be concisely expressed as

$$\boldsymbol{\Gamma}(\omega)\, \mathbf{a}(\omega) = \mathrm{e}^{i\omega T}\, \mathbf{d}^*(\omega), \tag{B7}$$

which has the exact form as eq. (12) we obtained for a point source in Section 2.2.

APPENDIX C: OPTIMIZED SOURCE IMAGING IN ACOUSTIC MEDIA

In Section 2.2, we formulated the OSI method for imaging a source in elastic media. Here, we show that this method is also applicable for imaging a source in acoustic media. Suppose an acoustic medium with receivers at $\mathbf{x}^i$ that sample a pressure wavefield associated with a source. Let $s(\mathbf{x}, t)$ denote the spatio-temporal source function defined over all space and time such that it can be nonzero only for $\mathbf{x} \in W$ and $t \in [0, T]$. We can think of the source function as a succession of spatially impulsive sources that are applied with strength $s(\boldsymbol{\xi}, t)$ at each location $\boldsymbol{\xi}$ and write

$$s(\mathbf{x}, t) = \int s(\boldsymbol{\xi}, t)\, \delta(\mathbf{x}-\boldsymbol{\xi})\, \mathrm{d}\boldsymbol{\xi}\,. \tag{C1}$$

The data recorded by a station at $\mathbf{x}^i$ associated with this distribution of impulsive sources can then be written as

$$d^i(t) = \int s(\boldsymbol{\xi}, t) * G(\mathbf{x}^i, t; \boldsymbol{\xi}, 0)\, \mathrm{d}\boldsymbol{\xi}\,, \tag{C2}$$

where $G(\mathbf{x}^i, t; \boldsymbol{\xi}, \tau)$ is the Green function with the source at $\mathbf{x} = \boldsymbol{\xi}$. In the frequency domain, eq. (C2) becomes

$$d^i(\omega) = \int s(\boldsymbol{\xi}, \omega)\, G(\mathbf{x}^i; \boldsymbol{\xi}, \omega)\, \mathrm{d}\boldsymbol{\xi}\,. \tag{C3}$$

Having defined the source function and the data associated with it, we can now lay out the OSI optimization problem. We assume that the scalar source wavefield at the time of focus is proportional to the source function $s(\mathbf{x}, t)$, with unity as the proportionality constant. With this assumption, we define our goal as finding signals $a^i(t)$ such that the difference between the wavefield $\phi(\mathbf{x}, t) = a^i(t) * G(\mathbf{x}, t; \mathbf{x}^i, 0)$ and the time-reversed source function $s(\mathbf{x}, T-t)$ is minimum.

This can be achieved by minimizing an objective function defined as

$$J = \iint_W |\phi(\mathbf{x}, t) - s(\mathbf{x}, T-t)|^2 \mathrm{d}\mathbf{x}\, \mathrm{d}t, \tag{C4}$$

which can be expressed in the frequency domain as

$$J(\omega) = \int_W \Big| a^i(\omega)\, G(\mathbf{x}; \mathbf{x}^i, \omega) - \int \mathrm{e}^{i\omega T}\, s^*(\boldsymbol{\xi}, \omega)\, \delta(\mathbf{x}-\boldsymbol{\xi})\, \mathrm{d}\boldsymbol{\xi} \Big|^2 \mathrm{d}\mathbf{x}, \tag{C5}$$

for each frequency. Minimization (C5) with respect to $a^i(\omega)$ gives

$$\begin{aligned} a^j(\omega) \int_W G(\mathbf{x}; \mathbf{x}^i, \omega) G^*(\mathbf{x}; \mathbf{x}^j, \omega) \mathrm{d}\mathbf{x} &= \mathrm{e}^{i\omega T} \int s^*(\boldsymbol{\xi}, \omega)\, G^*(\boldsymbol{\xi}; \mathbf{x}^i, \omega)\, \mathrm{d}\boldsymbol{\xi} \\ &= \mathrm{e}^{i\omega T} \int s^*(\boldsymbol{\xi}, \omega)\, G^*(\mathbf{x}^j; \boldsymbol{\xi}, \omega)\, \mathrm{d}\boldsymbol{\xi}\,, \end{aligned} \tag{C6}$$

where in the last step we have used the reciprocity principle for the acoustic Green function. Using eq. (C3), eq. (C6) can be written as

$$a^j(\omega) \int_W G(\mathbf{x}; \mathbf{x}^i, \omega)\, G^*(\mathbf{x}; \mathbf{x}^j, \omega)\, \mathrm{d}\mathbf{x} = \mathrm{e}^{i\omega T}\, d^{i*}(\omega)\,, \tag{C7}$$

or more concisely

$$\boldsymbol{\Gamma}(\omega)\, \mathbf{a}(\omega) = \mathrm{e}^{i\omega T} \mathbf{d}^*(\omega)\,, \tag{C8}$$

where $\boldsymbol{\Gamma}$ is an $N \times N$ defined as

$$\boldsymbol{\Gamma}^{ij}(\omega) = \int_W G(\mathbf{x}; \mathbf{x}^i, \omega)\, G^*(\mathbf{x}; \mathbf{x}^j, \omega)\, \mathrm{d}\mathbf{x}, \tag{C9}$$

and $\mathbf{d}(\omega)$ is an $N \times 1$ vector with elements defined as eq. (C3), which is the frequency component of the data recorded by station at $\mathbf{x}^i$.